Journal of Power Sources 195 (2010) 6539–6548

Contents lists available at ScienceDirect

Journal of Power Sources

journal homepage: www.elsevier.com/locate/jpowsour

High efficiency chemical energy conversion system based on a methane catalytic decomposition reaction and two fuel cells: Part I. Process modeling and validation

Qinghua Liu[a], Ye Tian[a], Hongjiao Li[a], Lijun Jia[a], Chun Xia[a], Levi T. Thompson[b], Yongdan Li[a,*]

[a] Tianjin Key Laboratory of Catalysis Science and Technology and State Key Laboratory for Chemical Engineering (Tianjin University), School of Chemical Engineering, Tianjin University, Tianjin 300072, China
[b] Department of Chemical Engineering, University of Michigan, Ann Arbor, MI 48109-2136, United States

ARTICLE INFO

Article history:
Received 23 March 2010
Received in revised form 14 April 2010
Accepted 14 April 2010
Available online 21 April 2010

Keywords:
Methane catalytic decomposition
Direct carbon fuel cell
Solid oxide fuel cell
Gas turbine
Carbon dioxide
Modeling

ABSTRACT

A highly efficient integrated energy conversion system is built based on a methane catalytic decomposition reactor (MCDR) together with a direct carbon fuel cell (DCFC) and an internal reforming solid oxide fuel cell (IRSOFC). In the MCDR, methane is decomposed to pure carbon and hydrogen. Carbon is used as the fuel of DCFC to generate power and produce pure carbon dioxide. The hydrogen and unconverted methane are used as the fuel in the IRSOFC. A gas turbine cycle is also used to produce more power output from the thermal energy generated in the IRSOFC. The output performance and efficiency of both the DCFC and IRSOFC are investigated and compared by development of exact models of them. It is found that this system has a unique loading flexibility due to the good high-loading property of DCFC and the good low loading property of IRSOFC. The effects of temperature, pressure, current densities, and methane conversion on the performance of the fuel cells and the system are discussed. The CO_2 emission reduction is effective, up to 80%, can be reduced with the proposed system.

1. Introduction

Fuel cells are electrochemical devices that convert the chemical energy of a fuel directly into electrical power. They are attractive because of their high efficiencies, flexibility in size, quiet operation and low emissions [1,2].

Solid oxide fuel cells (SOFCs) are high temperature devices (873–1273 K) that have emerged as promising candidates for use in large-scale electricity generation and combined power-heat systems [3–7]. Methane is considered as one of the most suitable fuels for the SOFC power system, however, it has to be converted to hydrogen in an external or internal reformer using one of the following techniques: steam reforming (SR), partial oxidation (POX), or autothermal reforming (ATR) [8–11]. These reforming techniques suffer from deactivation of the catalysts due to coking.

Methane catalytic decomposition (MCD) is a simple process for the simultaneous production of CO_x-free hydrogen and pure carbon with attractive nano-structural features [12–19]. The heat requirement for per mole hydrogen production is only 37.8 kJ compared to 63.0 kJ for SR process. The hydrogen-rich product can be used directly to power a proton exchange membrane fuel cell because the unconverted methane is benign to the noble metal electrocatalyst [20]. If this gas stream is fed to a SOFC with an internal reformer, the overall efficiency can be further improved because of a decrease of the load for the circulation system and the high temperature nature of the SOFC. In addition, deactivation of the internal reforming solid oxide fuel cell (IRSOFC) anode due to coking is avoided because of the high hydrogen to methane ratio of the stream [21]. The carbon produced in this device can be captured directly into a molten carbonate salt stream [22] and then fed to a direct carbon fuel cell (DCFC).

A DCFC converts the chemical energy in the solid carbon directly into electrical energy [23–30]. The overall cell reaction is the same as that of carbon combustion. It is a thermodynamically favorable process with theoretical thermal efficiency approaching 100%, which is much higher than the other types of fuel cells. This is due to the almost zero entropy change of the reaction. DCFC produces much lower emissions than a conversional coal-burning power plant along with its much higher fuel utilization [23,31]. Furthermore the effluent is pure CO_2.

Steinberg developed a high efficiency energy conversion cycle by integrating a DCFC with a hydrogen plasma black reactor (HPBR) [22]. Fossil and biomass fuels are converted to electricity, hydrogen and liquid transportation fuels (gasoline and diesel). He suggested that this scheme is competitive with conventional

* Corresponding author. Tel.: +86 22 27405613; fax: +86 22 27405243.
E-mail address: ydli@tju.edu.cn (Y. Li).

0378-7753/$ – see front matter © 2010 Elsevier B.V. All rights reserved.
doi:10.1016/j.jpowsour.2010.04.047

Nomenclature

A	a kinetic parameter related with ohmic resistance ($\Omega\,m^2\,Pa^{0.67}$)
a_1	regression parameter
a_2	regression parameter
a_i	regression parameter
B	a kinetic parameter related with ohmic resistance (K)
b_i	regression parameter
C	a constant related with ohmic resistance of the contacts ($\Omega\,m^2$)
C_{CO_2}	bulk concentration of CO_2 ($mol\,m^{-3}$)
D	a kinetic parameter related with the electrolyte content of the matrix ($\Omega\,m^2$)
E_a	apparent activation energy of the electrolyte conductivity ($J\,mol^{-1}$)
F	Faraday's constant (96,487 $C\,mol^{-1}$)
f	a kinetic parameter related with ohmic resistance (K)
G	Gibbs free energy (J)
G^o	Gibbs free energy at the standard state (J)
H	enthalpy (J)
H^o	enthalpy at the standard state (J)
h	mole enthalpy ($J\,mol^{-1}$)
i	current (mA)
j	current density ($mA\,cm^{-2}$)
j_o	exchange current density ($mA\,cm^{-2}$)
j_o^o	concentration-independent exchange current density ($mA\,cm^{-2}$)
j_{lim}	limiting current density ($mA\,cm^{-2}$)
K_{CO_2}	mass transport coefficient ($m\,s^{-1}$)
K_{MCD}	thermodynamic equilibrium constant of methane catalytic decomposition reaction
n_i	mole flow rate of species i ($mol\,s^{-1}$)
P	power (W)
p_i	partial pressure of species i in gas phase (atm)
p_{ref}	reference pressure (atm)
r_i	resistance of component i (Ω)
R	gas constant (8.314 $J\,mol\,K^{-1}$)
T	temperature (K)
V	voltage (V)
V^o	reversible voltage at standard pressure and the operating temperature (V)
$V_{a,an}$	anode activation polarization loss (V)
$V_{a,cat}$	cathode activation polarization loss (V)
$V_{c,an}$	anode concentration polarization loss (V)
$V_{c,cat}$	cathode concentration polarization loss (V)
V_{oc}	open circuit voltage (V)
V_{ohm}	ohmic polarization (V)
z	numbers of charge transfer

Greek letters

α	apparent charge transfer-coefficient ($\alpha = 0.5$)
γ_{an}	a kinetic parameter related with anode exchange current density ($A\,cm^{-2}$)
γ_{cat}	a kinetic parameter related with cathode exchange current density ($A\,cm^{-2}$)
η_{AC}	air compressor efficiency
ρ_i	resistivity of component i ($\Omega\,cm$)
φ_{CH_4}	methane conversion (mol%)
δ_i	component thickness (m)

Superscript

o	standard state

Subscripts

a	activation
an	anode
c	concentration
cat	cathode
lim	limit
ohm	ohmic

integrated combined cycle (IGCC) plants for electricity generation and hydrogen production. Muradov and Veziroğlu proposed a fossil-based "hydrogen-carbon" infrastructure [32] in which the hydrogen stream is fed to a proton exchange membrane fuel cell (PEMFC) and the carbon product is used for several purposes including power generation with a DCFC. A highly efficient power generation process using natural gas and an integrated MCD reactor (MCDR)–DCFC–PEMFC was proposed by Li et al. [33].

In this paper, an energy conversion system integrating MCDR–DCFC–IRSOFC is proposed and validated. One of the major objectives is to design a hydrocarbon-fueled power system with a high efficiency and a low CO_2 emission. In part one, the basic flow sheet is defined and the mathematical models describing the MCDR, DCFC, and IRSOFC are developed. Another purpose of this work is to explore an approach for the analysis of a dual fuel cell or a multiple fuel cell system.

2. System layout

The flow sheet of the proposed system, with numbered streams, is presented in Fig. 1. The major components include a MCDR, a IRSOFC, a DCFC with molten carbonate electrolyte, a catalytic afterburner (AB), a air compressor (AC), a heat recovery steam generator (HRSG), two gas turbines (one gas turbine (GT) is used to drive the air compressor, and the other one (PT) is used to generate power), a carbon dioxide-air mixer (M1), a steam-gaseous fuel mixer (M2), a methane-DCFC exhaust heat exchanger (HX1), an air-DCFC exhaust heat exchanger (HX2), a gaseous fuel-AB exhaust heat exchanger (HX3), and a pump (P). The invertors are not shown in this figure.

In this system, methane is preheated in HX1 with the DCFC exhausts, which are also used to preheat the DCFC inlet air in HX2. The preheated CH_4 fuel is fed into the MCDR and decomposed to H_2 and carbon. The carbon materials are absorbed and transported by a molten carbonate stream into the DCFC anode, and consumed electrochemically there to release electrons and produce CO_2. A fraction of CO_2 (66.7 mol%) is sent to the DCFC cathode to regenerate the carbonate after mixing with air (CO_2/O_2 ratio 2:1) in M1. The rest CO_2 (33.3 mol%) is used to preheat air and CH_4. The gaseous products containing H_2 generated in the MCDR and unconverted CH_4 are fed into the IRSOFC anode after mixing with steam in M2. As shown in Fig. 2, the internal reforming reaction occurs in the IRSOFC anode compartment. Methane is converted into H_2. Air is compressed in the AC and preheated in the HX3 and fed into the IRSOFC cathode. The SOFC cell reaction is exothermic, and the heat generated is partially used to drive the internal reforming reaction. The O_2 depleted air and the unreacted gaseous fuel are burned in the AB. The exhaust emitted from the AB can be further utilized to offer shaft work for the air compressor in the GT and generate power in the PT. Finally, this stream is used to preheat the air entering the IRSOFC cathode and generate steam in the HRSG, respectively. It is assumed that there is no heat transfer with the surroundings in above processes.

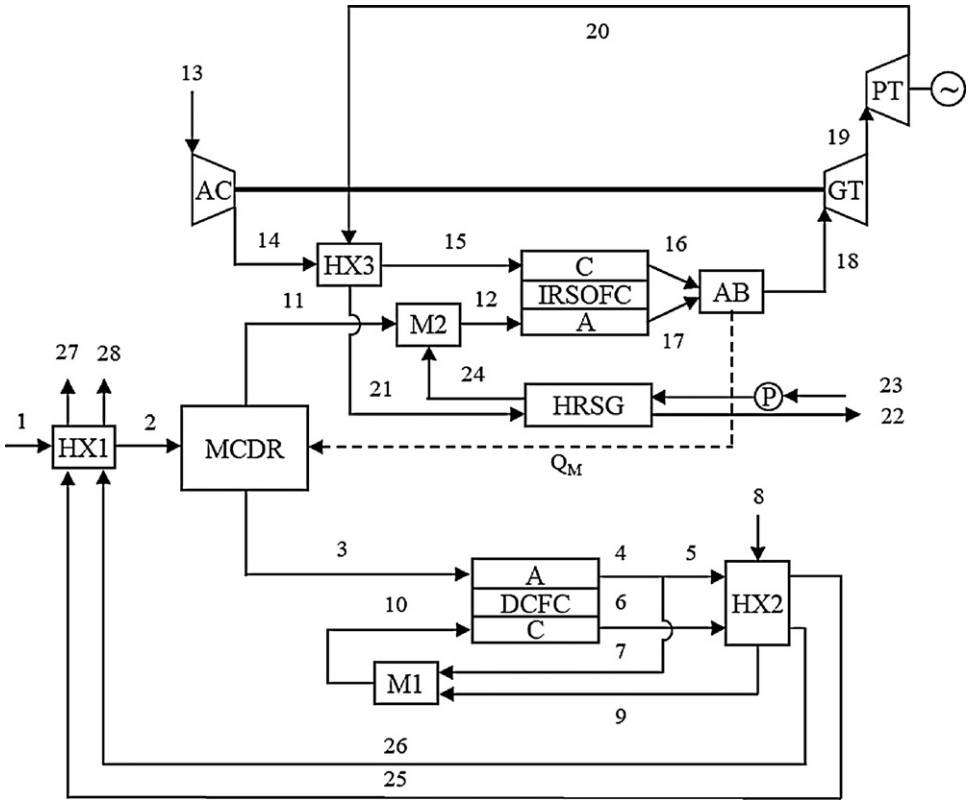

Fig. 1. A schematic diagram of the proposed system.

3. Methane catalytic decomposition reactor model

The CH_4 decomposition reaction is a moderately endothermic reaction that proceeds as follows:

$$CH_4 \rightarrow C + 2H_2 \qquad \Delta H^o = 75.6\,\text{kJ mol}^{-1} \tag{1}$$

The composition of the gaseous stream and CH_4 conversion can be determined using the definitions of the equilibrium constant K_{MCD}:

$$K_{MCD} = \frac{p_{H_2}^2}{p_{CH_4}} \tag{2}$$

$$\text{Methane conversion}: \quad \varphi_{CH_4} = \frac{n_{H_2,\text{out,MCDR}}}{2n_{CH_4,\text{in,MCDR}}} \tag{3}$$

Due to a very strong C–H bond (440 kJ mol^{-1} at standard state), CH_4 is one of the most stable organic molecules. Thermal decomposition of methane requires a temperature higher than 1273 K [13,32]. A number of transition metal and carbon catalysts have been investigated to reduce the working temperature for CH_4 decomposition [12–19,34,35]. In this work, a carbon catalyst is selected for several reasons. (I) The product carbon has high electrochemical activity. The material produced using carbon catalyst contains mainly carbon filaments and turbostatic carbon. It has been reported that turbostatic carbon has very good electrochemical activity as a fuel for DCFC [23]. Filamentous carbon is also highly active [23,24]. (II) No further purification step is needed when using this fuel [10–17]. (III) The work temperature for the carbon catalysts matches that of the fuel cells used in this work. The MCDR based on carbon catalysts are often operated at 1073–1273 K. The IRSOFC and DCFC are often operated at 1073–1273 K, and 873–1073 K, respectively. (IV) Finally there are economical reasons for using carbon. The cost for carbon catalysts is substantially lower than that for metal catalysts [14,17,21,36].

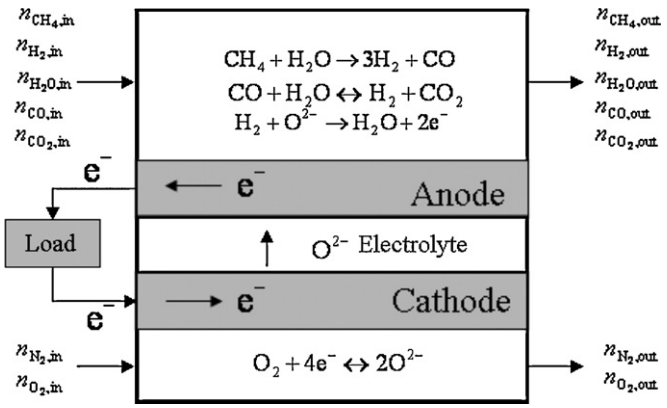

Fig. 2. A schematic diagram of the IRSOFC.

In order to achieve continuous H_2 and carbon production, a fluidized bed reactor (FBR) is chosen for the MCD reaction [37–40]. Fig. 3 illustrates the FBR for the MCD process. Preheated dry CH_4 is decomposed over the carbon catalyst. The heat required, Q_M, is supplied directly by the afterburner.

4. Direct carbon fuel cell model

A DCFC model was developed in order to predict the polarizations, operating voltage, power output, and exhaust temperature. This new model is an improvement of the models we used in the past [41]. DCFCs under development are of three types based on the electrolytes used: solid oxide, molten sodium hydroxide, and molten carbonate [23–29]. Fig. 4 presents a DCFC based on a molten carbonate electrolyte. The overall cell reaction for the DCFC is:

$$C + O_2 \rightarrow CO_2 \qquad \Delta H^o = -393.5\,\text{kJ mol}^{-1} \tag{4}$$

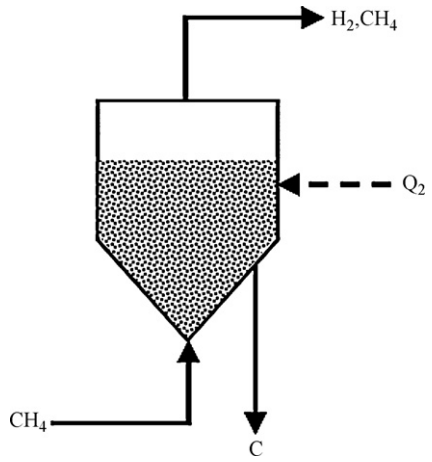

Fig. 3. A schematic diagram of the FBR for the MCD reaction.

This reaction is extremely exothermic. The carbon fuel and oxidant are introduced into two individual chambers separated by electrolyte membrane. At the anode side of the molten carbonate electrolyte based DCFC, carbon is electrochemical oxidized by CO_3^{2-} anions following the reaction:

$$C + 2CO_3^{2-} \rightarrow 3CO_2 + 4e^- \quad (5)$$

The carbonate ion (CO_3^{2-}) is generated at the cathode according to:

$$2CO_2 + O_2 + 4e^- \rightarrow 2CO_3^{2-} \quad (6)$$

and is transferred through the electrolyte membrane to the anode. This type of DCFC can use the same cathode and electrolyte materials as a molten carbonate fuel cell (MCFC) [23]. The cell details and operating parameters are summarized in Table 1.

The open circuit voltage (OCV) of DCFC can be calculated using the Nernst equation.

$$V_{oc,DCFC} = V^o_{DCFC} + \frac{RT}{zF} \ln\left(\frac{p_{O_2} p^2_{CO_2,cat}}{p^3_{CO_2,an}}\right) = \frac{\Delta G^o_{DCFC}}{zF} + \frac{RT}{zF} \ln\left(\frac{p_{O_2} p^2_{CO_2,cat}}{p^3_{CO_2,an}}\right) \quad (7)$$

where V^o_{DCFC} is the reversible voltage at the standard pressure and operating temperature, ΔG^o_{DCFC} is the Gibbs free energy change of reaction (4), and z is the number of electrons transferred in the reaction (here $z = 4$). The voltage is reduced by the polarization losses,

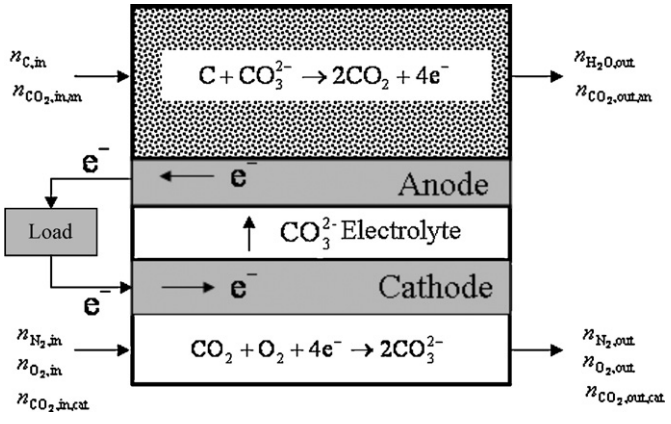

Fig. 4. A schematic diagram of a DCFC based the molten carbonate electrolytes.

Table 1
Operating parameters.

Parameters	Values
MCDR	
Operating temperature (K)	1073–1273
Methane inlet molar flow rate (mol s^{-1})	1.0
DCFC	
Operating temperature (K)	873–1073
Operating pressure (atm)	1.0
Fuel utilization (%)	100
Air utilization (%)	50
CO_2 utilization in the cathode (%)	100
Anode materials	Ni
Anode thickness (m)	0.5×10^{-3}
Cathode	$Li_xNi_{1-x}O$
Cathode thickness (m)	0.5×10^{-3}
Electrolyte (mol%)	$62Li_2CO_3/38K_2CO_3$
Matrix materials	γ-$LiAlO_2$
Matrix thickness (m)	0.5×10^{-3}
IRSOFC	
Operating temperature (K)	1073–1273
Operating pressure (atm)	1.0
Fuel utilization (%)	80.00
Air utilization (%)	30.00
Steam to carbon ratio	2.2:1.0
Limiting current density (mA cm^{-2})	900
Anode	Nickel/yttria-stabilized zirconia
Cathode	LSM composite electrolyte
Electrolyte	Yttria-stabilized zirconia
$E_{act,an}$ ($\times 10^3$ J mol^{-1})	120
$E_{act,cat}$ ($\times 10^3$ J mol^{-1})	120
γ_{an} ($\times 10^9$ mA cm^{-2})	5.5
γ_{cat} ($\times 10^8$ mA cm^{-2})	7.0
Other components	
AC efficiency (%)	81
GT efficiency (%)	84
PT efficiency (%)	89
HRSG efficiency (%)	80
Heat exchanger effectiveness (%)	98
Catalytic afterburner efficiency (%)	100

namely: anode and cathode activation polarizations ($V_{a,an}$, $V_{a,cat}$); ohmic polarizations for each components (V_{ohm}); anode and cathode concentration polarizations ($V_{c,an}$, $V_{c,cat}$). The operating voltage for the fuel cell (V) is calculated by subtracting the various polarizations from the open circuit voltage (OCV).

$$V = V_{oc} - V_{a,an} - V_{a,cat} - V_{ohm} - V_{c,an} - V_{c,cat} \quad (8)$$

The power output is calculated as:

$$P = iV \quad (9)$$

The activation polarization is caused by the slow electron release or capture steps in the electrode–electrolyte bi-layers. Generally, it can be determined using the Bulter–Volmer equation, as follows:

$$j = j_o \left[\exp\left(\alpha \frac{zF}{RT} V_a\right) - \exp\left(-(1-\alpha)\frac{zF}{RT} V_a\right)\right] \quad (10)$$

where α is the apparent charge transfer-coefficient which is often taken as 0.5. The activation polarization depends on the exchange current density (j_o) since it is a measure of the electrochemical kinetics. The exchange current density of the cathode semi-reaction is determined by the following equation based on the peroxide mechanism [42].

$$j_{o,cat} = j^o_{o,cat} (p_{CO_2,cat})^{a_1} (p_{O_2,cat})^{a_2} \quad (11)$$

where $j^o_{o,cat}$ is the concentration-independent exchange current density, $p_{CO_2,cat}$ and $p_{O_2,cat}$ the partial pressures of CO_2 and O_2 in the cathode, respectively. The coefficients a_1 ($a_1 = 0.375$) and a_2 ($a_2 = -1.25$) are taken from Ref. [42].

The evaluation of the anode exchange current density is complicated due to its dependence on electrode structure, carbon material properties and reaction mechanisms. There are few models that consider the kinetics of carbon electrochemical oxidation in molten carbonates [38,40]. A literature investigation suggests that the $j_{o,an}$ for pyrolytic graphite is of the order of 0.01–1.0 mA cm^{-2} at 873–1073 K [27]. According to Cherepy et al. [23], the higher the crystallographic disorder, *viz.* the less graphitization, the higher the electrochemical reactivity. Therefore, the MCD carbon materials should have a much higher value for $j_{o,an}$ compared to that of pyrolytic graphite. In this work, the values of the $j_{o,an}$ are taken from [27] but multiplied by a factor in the range of 1–2.

The ohmic polarization is caused by resistances of the electrodes, electrolytes and inter-contacts. These are functions of temperature and can be evaluated using the following equation [41,43].

$$r = \frac{A}{p_{O_2}^{0.67}} \exp\left(\frac{B}{T}\right) + C + D\exp\left(\frac{f}{T}\right) \quad (12)$$

where p_{O_2} is the partial pressure of oxygen at cathode surface, A and B are kinetic parameters related to the ohmic resistances, C is a constant related to the ohmic resistance of the contacts, and D is a kinetic parameter that is proportional to the electrolyte content of the matrix. The total ohmic polarization is:

$$V_{ohm} = ir \quad (13)$$

The concentration polarization is determined by a limiting current density method and is described as follows [44]

$$V_c = \frac{RT}{zF} \ln\left(1 - \frac{j}{j_{lim}}\right) \quad (14)$$

where j_{lim} is the limiting current density caused by limited diffusion of gaseous reactants and product species into and out of the porous electrodes. The cathode concentration polarization is calculated as

$$j_{lim,cat} = zFK_{CO_2}C_{CO_2} \quad (15)$$

where C_{CO_2} is the bulk concentration of CO_2. The mass transport coefficient K_{CO_2} is taken as 3.5×10^{-2} m s^{-1} [45]. There are no porous electrodes used in the anode of the proposed DCFC. In additional, the diffusion resistance of CO_3^{2-} anion in and CO_2 out of the carbon particle is small. In this work, the limiting current density of anode is assumed to be 1.0×10^3 mA cm^{-2}.

5. Internal reforming solid oxide fuel cell model

A schematic presentation of an IRSOFC is provided in Fig. 2. The reforming reactions take place in the anode chamber and are as follows:

Methane steam-reforming reaction:

$$CH_4 + H_2O(g) \rightarrow CO + 3H_2 \qquad \Delta H^o = 206.2\ \text{kJ mol}^{-1} \quad (16)$$

Water–gas shift reaction:

$$CO + H_2O(g) \leftrightarrow CO_2 + H_2 \qquad \Delta H^o = -41.1\ \text{kJ mol}^{-1} \quad (17)$$

These reactions are assumed to be at or very close to equilibrium. Steam is provided externally by a vaporizer. The CH_4 steam-reforming reaction is endothermic and the heat required is supplied by the overall cell reaction.

$$H_2 + (1/2)O_2 \rightarrow H_2O(g) \qquad \Delta H^o = -241.8\ \text{kJ mol}^{-1} \quad (18)$$

The H_2 produced in the MCDR and in the reforming process are electrochemically oxidized by O^{2-} in the three phase boundary in the anode side to produce steam and release electrons.

$$H_2 + O^{2-} \rightarrow H_2O(g) + 2e^- \quad (19)$$

Table 2
The resistivity constants of all components in the IRSOFC.

Components	a ($\times 10^{-5}$ Ω cm)	b (K)	δ ($\times 10^{-6}$ m)
Anode	2.98	−1392	150
Cathode	8.11	600	2000
Electrolyte	2.94	10350	40
Interconnector	125.6	4690	100

At the same time, O^{2-} is regenerated with the cathode semi-reaction as:

$$(1/2)O_2 + 2e^- \rightarrow O^{2-} \quad (20)$$

The OCV of the IRSOFC can be calculated using Nernst equation.

$$V_{oc,SOFC} = V^o_{SOFC} + \frac{RT}{zF} \ln\left(\frac{p_{H_2}\sqrt[2]{p_{O_2}}}{p_{H_2O}}\right) = \frac{\Delta G^o_{SOFC}}{zF} + \frac{RT}{zF}\ln\left(\frac{p_{H_2}\sqrt[2]{p_{O_2}}}{p_{H_2O}}\right) \quad (21)$$

where z is 2. The IRSOFC suffers from various polarization losses and the operating voltage follows Eq. (8).

Eq. (10) is applied to both the anode and cathode semi-reactions in order to evaluate their activation polarizations in the IRSOFC. The activation polarizations depend principally on the exchange current density. The following equations are used for evaluate the anode and the cathode exchange current densities, respectively [46,47].

$$j_{o,an} = \gamma_{an}\left(\frac{p_{H_2}}{p_{ref}}\right)\left(\frac{p_{H_2O}}{p_{ref}}\right) \exp\left(-\frac{E_{a,an}}{RT}\right) \quad (22)$$

$$j_{o,cat} = \gamma_{cat}\left(\frac{p_{O_2}}{p_{ref}}\right)^{0.25} \exp\left(-\frac{E_{a,cat}}{RT}\right) \quad (23)$$

The ohmic polarization for the IRSOFC is a function of temperature and can be reduced by operating at high temperatures. Generally, the ohmic polarization is determined experimentally from the measured temperature dependency of the resistivity [46,47]. It is can be calculated using the following equations:

$$V_{ohm} = \sum_i ir_i \quad (24)$$

$$r_i = \delta_i\rho_i \quad (25)$$

$$\rho_i = a_i \exp\left(\frac{-b_i}{T}\right) \quad (26)$$

where r_i is the component resistances, δ_i is the component thickness, ρ_i is the component resistivities, and a_i and b_i are the parameters obtained by experimental regression. The values for each of the component parameters are list in Table 2 [47].

Hydrogen is consumed by the anode semi-reactions at the three-phase boundary. Its partial pressure decreases when it is not readily replenished from the bulk gas phase. This causes concentration polarization in the anode and decreases the cell voltage. The same phenomenon occurs at the cathode where oxygen is consumed by the cathode semi-reaction. In this work, the concentration polarization is determined using the limiting current density method given by Eq. (14) with the assumption of a constant value for limiting current density [47].

6. Models of other components

In order to reach high CH_4 conversion and effective utilization of the catalyst, the MCDR operating temperature has to be higher than 1073 K [15]. The CH_4 stream must be preheated before entering

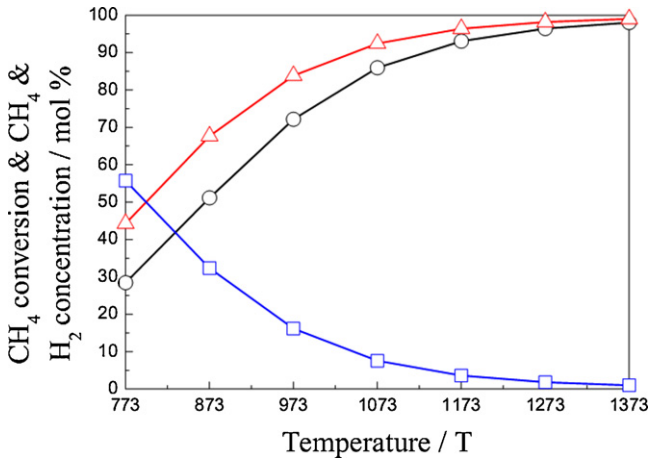

Fig. 5. Equilibrium conversions for CH_4 and equilibrium concentrations for H_2 and CH_4 at atmospheric pressure and varying temperatures. (○) CH_4 conversion, (△) H_2 concentration, (□) CH_4 concentration.

the reactor. The carbon products are fed directly into DCFC without preheating. The gaseous products are mixed with steam in M2. This high temperature stream is fed into the IRSOFC anode without significant temperature gradients [48]. The effectiveness of all heat exchangers is assumed to be 98% [47,49].

The AC, GT and PT are all under adiabatic operation. The work input in the AC is calculated using following equation.

$$P_c = \frac{n_{air}(h_{AC2} - h_{AC1})}{\eta_{AC}} \quad (27)$$

where n_{air} is the mole flow rate of air, h_{AC2} and h_{AC1} are the mole enthalpies of air of outlet and inlet, respectively, η_{AC} is the air compressor efficiency. The work output of GT and the power output of PT are equal to the products of the enthalpy change of the exhausts multiplied with the efficiency of turbines.

The catalytic afterburner is modeled on the basis of the complete fuel (including H_2, CO and CH_4) oxidation. The burner is under adiabatic operation and the outlet gas temperature is calculated using simple mass and energy balances.

Finally, it is assumed that there are no chemical reactions occurring in the mixers and HRSG. Mass and energy balances for the mixers and the HRSG are used to determine the mole flow rates and outlet temperatures.

For the DCFC and IRSOFC, the characteristics including voltage efficiency, current efficiency (fuel utilization efficiency), theoretical reversible efficiency, and overall cell efficiency were estimated [45].

Additional assumptions are listed as follows:

- Steady state operation for all components with negligible friction loss.
- All gases, e.g. CH_4, CO, CO_2, H_2O, H_2, N_2, and O_2, are ideal gases. The air contains 21 mol% O_2 and 79 mol% N_2.
- The operation pressure of MCDR and DCFC is 1 atm with negligible pressure loss.

7. Results and discussion

7.1. Effects of CH_4 conversion

Fig. 5 presents the equilibrium conversions of CH_4 and equilibrium concentrations of H_2 and CH_4 at atmospheric pressure with varying temperatures. For temperatures higher than 973 K, the CH_4 conversion is higher than 80%. Because the carbon product is used for power generation, a high CH_4 conversion is preferable. As defined above, the MCDR operation temperature is in the range

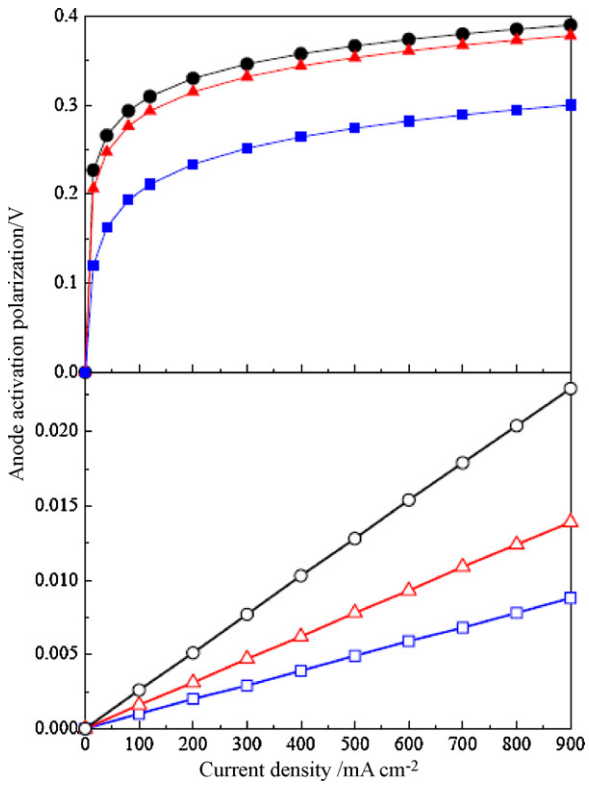

Fig. 6. The anode activation polarization curves for the DCFC at (●) 923 K, (▲) 973 K, (■) 1023 K (top) and IRSOFC at (○) 1173 K, (△) 1223 K, (□) 1273 K (bottom). The operating pressure is 1.0 atm.

of 1073–1273 K. It is higher than the DCFC operating temperature (873–1073 K) and similar to that for the IRSOFC (1073–1273 K). The MCD is a high temperature O_2-free process at steady state, consequently, the high temperature carbon product exiting from the MCDR can be directly fed into the DCFC anode.

The electrical efficiency of the energy system increases 5% when the CH_4 conversion increases from 50 to 90%. This stems from the significant increase of the DCFC power output as the amount of carbon fuel increases along with the CH_4 conversion. In contrast, the IRSOFC power generation decreases with increasing CH_4 conversion due to the trade-off between the MCD and the internal reforming (IR) processes. As the CH_4 conversion increases in the MCDR, the amount of residual CH_4 decreases, *viz.* the amount of CH_4 taking part in the reforming reaction decreases. Hydrogen produce with the reforming process is twice as high as that with the MCD process. Consequently, the net amount of H_2 taking part in the anode reaction decreases. This causes the power output and the electric efficiency of the IRSOFC to decrease with increasing CH_4 conversion in the MCDR step.

7.2. Properties of DCFC and IRSOFC

7.2.1. Polarization losses of DCFC and IRSOFC

The anode and cathode activation polarizations for the DCFC and IRSOFC are displayed in Figs. 6 and 7, respectively. The results indicate that the DCFC anode activation polarization is of the order of magnitude of 10^{-1} V, while the IRSOFC anode activation polarization is in the range of 10^{-3} to 10^{-2} V for IRSOFC anode. This is caused by the lower exchange current density for the DCFC anode which is in the range of 0.1–2 mA cm^{-2} at 873–1023 K [27,50]. Nevertheless, the figure clearly shows that both the anode activation polarizations for the DCFC and IRSOFC decrease with the increase in the operating temperatures. As shown in Fig. 7, cathode acti-

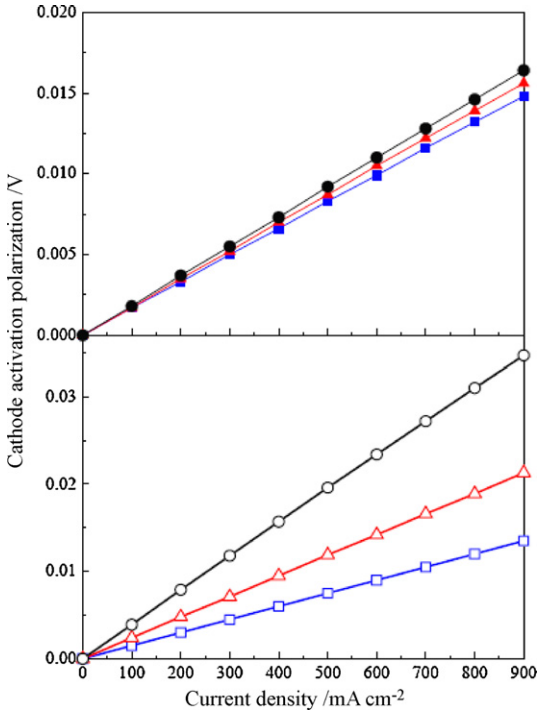

Fig. 7. Cathode activation polarization curves. DCFC at (●) 923 K, (▲) 973 K, (■) 1023 K (top) and IRSOFC at (○) 1173 K, (△) 1223 K, (□) 1273 K (bottom). The operating pressure is 1.0 atm.

vation polarizations for the DCFC and IRSOFC are lower and both in the range of 10^{-3} to 10^{-2} V. In addition, they depend on the operating temperature and the current density. Fig. 8 illustrates the ohmic polarizations for the DCFC and IRSOFC. They increase

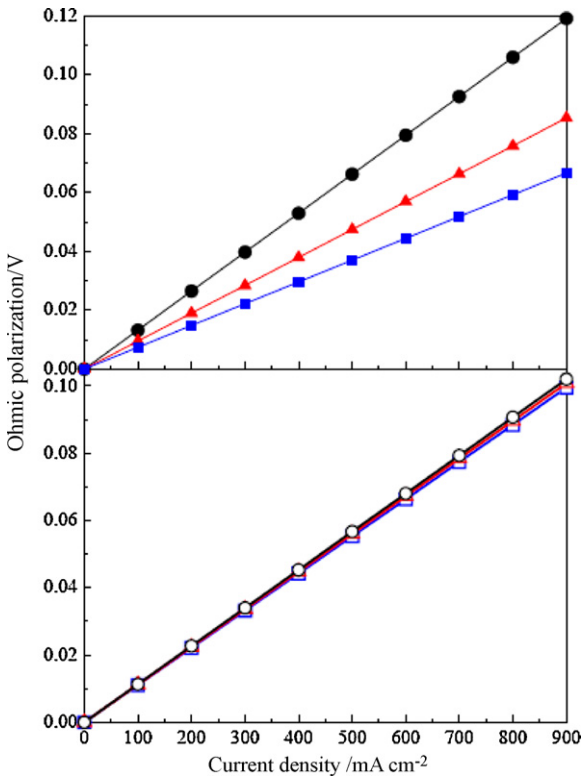

Fig. 8. Ohmic polarization curves. DCFC at (●) 923 K, (▲) 973 K, (■) 1023 K (top) and IRSOFC at (○) 1173 K, (△) 1223 K, (□) 1273 K (bottom). The operating pressure is 1.0 atm.

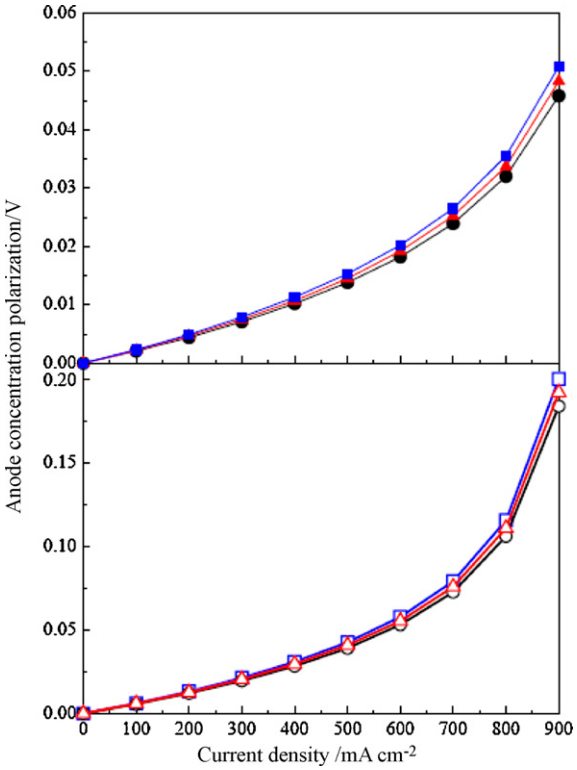

Fig. 9. Anode concentration polarization curves. DCFC at (●) 923 K, (▲) 973 K, (■) 1023 K (top) and IRSOFC at (○) 1173 K, (△) 1223 K, (□) 1273 K (bottom). The operating pressure is 1.0 atm.

linearly with the increases in the current density. Although the IRSOFC operating temperature is higher than that for the DCFC, the ohmic polarizations are as high as the DCFC due to the low ionic conductivity of the electrolyte (*viz.* yttria-stabilized zirconia electrolyte) and the low electronic conductivity of the interconnectors [51]. Fig. 9 shows that the anode concentration polarizations for the DCFC and IRSOFC are less than 0.02 V when the current density is less than 600 mA cm^{-2} and increase sharply at high current densities. Fig. 10 illustrates the DCFC and IRSOFC cathode concentration polarizations. Concentration polarizations for the DCFC are much lower than those for the IRSOFC due to the higher limiting current density.

7.2.2. *Electrochemical performance of DCFC and IRSOFC*

The DCFC and IRSOFC are the main units in the proposed system and determine the power output and heat generation for the system. Fig. 11 illustrates the DCFC and IRSOFC OCVs at different temperatures. The OCV depends on Gibbs free energy change (ΔG) for the cell reactions, and the partial pressure of the gaseous reactants and products. For the DCFC, the OCV is 0.94 V due to the nearly constant ΔG^o value (approximately −395 kJ mol^{-1} at 873–1073 K). For the IRSOFC, the ΔG^o decreases from 188.5 to 177.3 kJ mol^{-1} which results in a decrease in the OCV from 0.85 to 0.80 V in the same temperature range. This decrease can be moderated by increasing the operating pressure.

Figs. 12 and 13 display the kinetic properties and the power densities of the DCFC and IRSOFC at different temperatures. The DCFC cell voltage decreases to 0.6–0.7 V due to the large anode activation polarization losses at 923–1023 K and current densities less than 100 mA cm^{-2}. Then it decreases slowly along with the increase of the current density in a large range (100–900 mA cm^{-2}). The power density of DCFC increases almost linearly with increases in the current density at 923–1023 K. It is also clearly shown that the DCFC

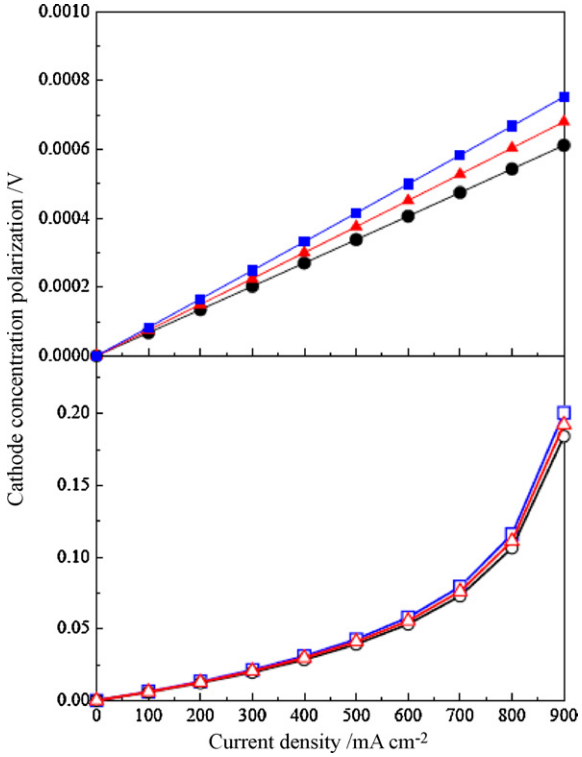

Fig. 10. Cathode concentration polarization curves. DCFC at (●) 923 K, (▲) 973 K, (■) 1023 K (top) and IRSOFC at (○) 1173 K, (△) 1223 K, (□) 1273 K (bottom). The operating pressure is 1.0 atm.

performance can be improved by increasing the operating temperature. For the IRSOFC, the cell voltage decrease is small in the range of 0–600 mA cm^{-2} at 1173–1273 K, however, a significant voltage decrease occurs at higher current densities due to depletion of the H_2 fuel. This reveals that the IRSOFC is favored at relatively low current densities (<400 mA cm^{-2}), while the DCFC performance is better at high current densities (>400 mA cm^{-2}). The combination of the DCFC and IRSOFC increases the loading flexibility.

In order to evaluate the proposed system comprehensively, a comparison of DCFC and IRSOFC was made. In particular, the various efficiencies including the theoretical reversible efficiency, voltage efficiency, current efficiency, and overall cell efficiency were estimated. The results are shown in Fig. 14. The theoretical reversible efficiency for the DCFC is almost 100% at 873–1073 K,

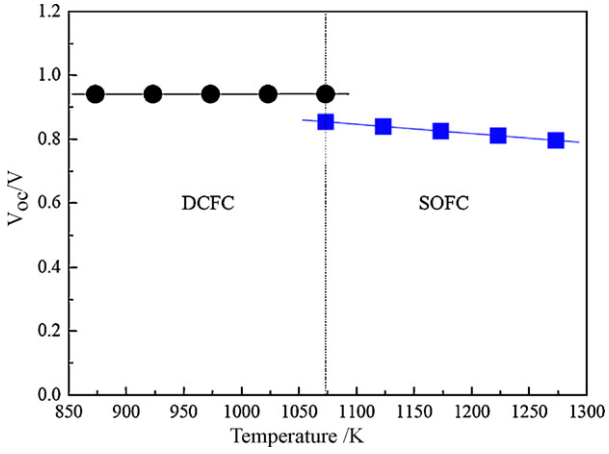

Fig. 11. Open circuit voltages for the DCFC and IRSOFC at different temperatures. The operating pressure is 1.0 atm.

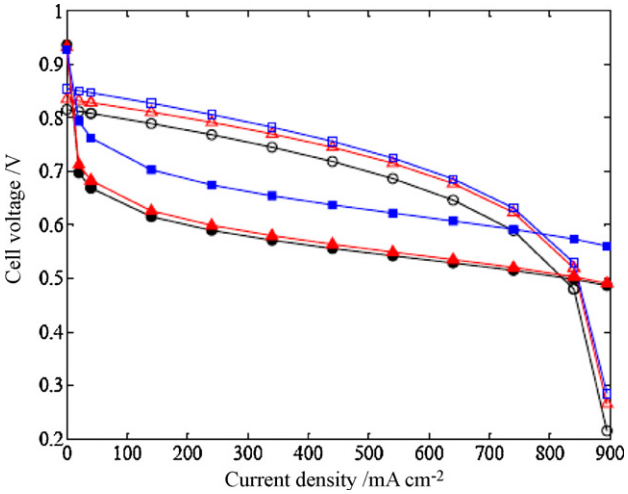

Fig. 12. The cell voltage as a function of current density for the DCFC at (●) 923 K, (▲) 973 K, (■) 1023 K, and IRSOFC at (○) 1173 K, (△) 1223 K, (□) 1273 K. The operating pressure is 1.0 atm.

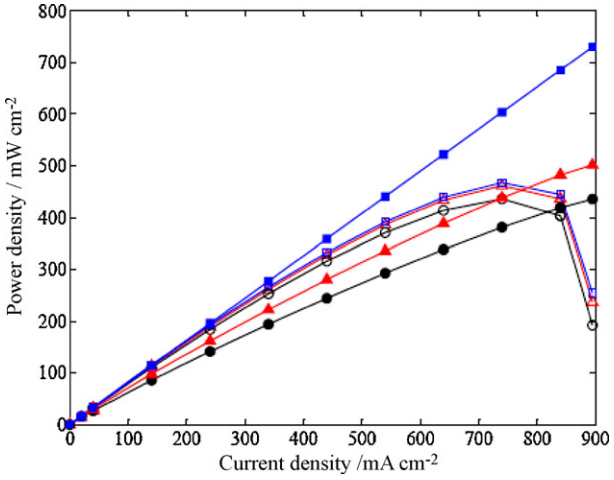

Fig. 13. The power densities as a function of the current density for the DCFC at (●) 923 K, (▲) 973 K, (■) 1023 K and IRSOFC at (○) 1173 K, (△) 1223 K, (□) 1273 K. The operating pressure is 1.0 atm.

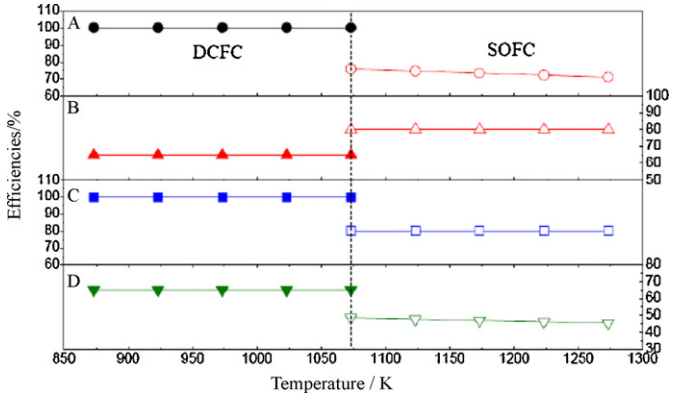

Fig. 14. A comparison of efficiencies for the DCFC and IRSOFC. (A) theoretical reversible efficiencies, (B) voltage efficiencies, (C) current efficiencies, (D) overall cell efficiencies. The operating pressure is 1.0 atm.

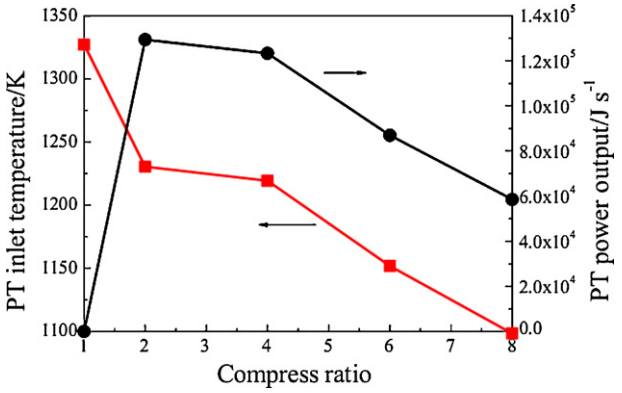

Fig. 15. The effect of air compress ratio on the PT inlet temperature and PT power outlet.

while that for the IRSOFC is 70–80% at 1073–1273 K. The voltage efficiency for the DCFC is somewhat lower due to the large polarization losses. However, the DCFC has higher current efficiencies because of the total consumption and undiluted concentration of the solid carbon fuel. The overall cell efficiency for the DCFC is approximately 65% at 873–1073 K. For the IRSOFC, the overall cell efficiency is in the range of 45–50% at 1073–1273 K under the operating pressure of 1 atm.

7.2.3. Operating pressure of IRSOFC

As shown in Eqs. (21) and (23), the voltage output of IRSOFC can be improved with the increase of the OCV and the decrease of cathode activation polarization loss with increasing the partial pressure of oxygen fed into the IRSOFC cathode. Therefore, air is compressed through the air compressor to raise the power output of the IRSOFC. There is a trade-off between shaft work output from GT and the power output from PT. Along with the increase of the air compress ratio, the shaft work output from GT increases, the temperature and pressure of the gases at the GT outlet or the PT input decrease. While, as shown in Fig. 15, the power output from PT increase to the peak value at the compress ratio of 2. The sum of power output of IRSOFC and PT is given in Fig. 16. It is clearly shown that the maximum power output is achieved at the compress ratio of 4.

7.3. Reduction of CO_2 emissions

In a typical SOFC based integrated energy system, the separation and recovery of CO_2 from the exhaust stream is a multi-step and capital intensive process [4,49,52]. In the system proposed here, the principal CO_2 generator is the DCFC anode and this CO_2 can be easily captured and recovered. Only a small fraction of the CO_2 is generated from the IRSOFC anode. Compared to a typical SOFC based integrated energy system, the emission of CO_2 is reduced dramatically. The major factors that affect the emissions of CO_2 is CH_4 conversion in the MCDR and the current output in the DCFC. In this case, a 80% reduction of CO_2 emission can be achieved.

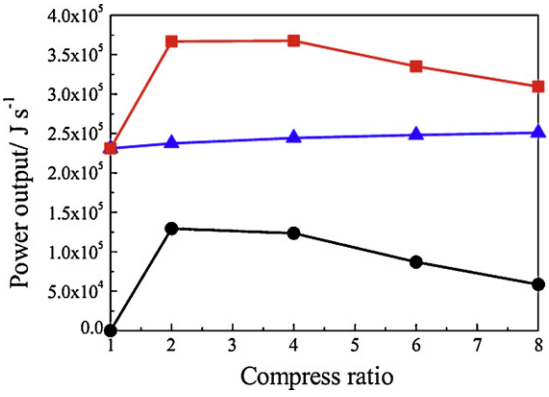

Fig. 16. The effect of air compress ratio on the power output of PT and IRSOFC, (●) PT, (▲) IRSOFC, (■) PT and IRSOFC.

8. Conclusions

In this work, a highly efficient power system that integrates a MCDR, a DCFC, a IRSOFC and two GTs is designed and simulated.

The results show that CH_4 conversion plays a major role with regard to the power output of the overall system. The performances of DCFC and IRSOFC were evaluated using electrochemical models. The results indicate that they are under anode activation polarization and ohmic polarization control, respectively. The DCFC has better high-load performance while IRSOFC performs better at relatively lower loads. Thus the proposed system offers significant load flexibility. The pressure of air inlet in the IRSOFC cathode affects the power output of the IRSOFC and the power turbine. The optimum air compress ratio is 4. The production of pure CO_2 saves the cost of its sequestration and facilitates its utilization for other industrial processes. In this work, 80% of the CO_2 emission is reduced compared to a system utilizing a single SOFC. A further exploration of this system with exergy analysis will be discussed in a following article.

Acknowledgements

This work has been supported by the Natural Science Foundation of China under contract numbers 20425619 and 20736007. The work has been also supported by the Program of Introducing Talents to the University Disciplines under file number B06006, and the Program for Changjiang Scholars and Innovative Research Teams in Universities under file number IRT 0641.

References

[1] M. Winter, R.J. Brodd, Chem. Rev. 104 (2004) 4245–4269.
[2] K.V. Kordesch, G.R. Simader, Chem. Rev. 95 (1995) 191–207.
[3] J. Padulled, G.W. Ault, J.R. McDonald, J. Power Sources 86 (2000) 495–900.
[4] P. Costamagna, A. Selimovic, M. Del Borghi, Chem. Eng. J. 102 (2004) 61–69.
[5] Y.D. Li, Z.B. Rui, C. Xia, M. Anderson, Y.S. Lin, Catal. Today 148 (2009) 303–309.
[6] C. Xia, Y. Li, Y. Tian, Q.H. Liu, Y.C. Zhao, L.J. Jia, Y.D. Li, J. Power Sources 188 (2009) 156–162.
[7] C. Xia, Y. Li, Y. Tian, Q.H. Liu, Z.M. Wang, L.J. Jia, Y.C. Zhao, Y.D. Li, J. Power Sources 195 (2010) 3149–3164.
[8] J.N. Armor, Appl. Catal. A 176 (1999) 159–176.
[9] J.B. Claridge, A.P.E. York, A.J. Brungs, C. Marquez-Alvarez, J. Sloan, S.C. Tsang, M.L.H. Green, J. Catal. 180 (1998) 85–100.
[10] S. Freni, G. Calogero, S. Cavallaro, J. Power Sources 87 (2000) 28–38.
[11] N.Z. Muradov, Energy Fuels 12 (1998) 41–48.
[12] M. Steinberg, Int. J. Hydrogen Energy 24 (1999) 771–777.
[13] N.Z. Muradov, T.N. Veziroglu, Int. J. Hydrogen Energy 30 (2005) 225–237.
[14] T.V. Choudhary, C. Sivadinarayana, C.C. Chusuei, A. Klinghoffer, D.W. Goodman, J. Catal. 199 (2001) 9–18.
[15] Y.D. Li, J.L. Chen, Y.N. Qin, L. Chang, Energy Fuels 14 (2000) 1188–1194.
[16] L.Y. Piao, Y.D. Li, J.L. Chen, L. Chang, J.Y.S. Lin, Catal. Today 74 (2002) 145–155.
[17] J.L. Chen, Y.H. Qiao, Y.D. Li, Appl. Catal. A 337 (2008) 148–154.
[18] J.L. Chen, Q. Ma, T.E. Rufford, Y.D. Li, Z.H. Zhu, Appl. Catal. A 362 (2009) 1–7.
[19] D.X. Li, J.L. Chen, Y.D. Li, Int. J. Hydrogen Energy 34 (2009) 299–307.
[20] A.K. Avci, D.L. Trimm, Z.I. Önsan, Chem. Eng. J. 90 (2002) 77–87.
[21] J.T. Richardson, Principles of Catalyst Development, Plenum Press, New York, USA, 1989.
[22] M. Steinberg, Int. J. Hydrogen Energy 31 (2006) 405–411.
[23] N.J. Cherepy, R. Krueger, K.J. Fiet, A.F. Jankowski, J.F. Cooper, J. Electrochem. Soc. 152 (2005) 80–87.
[24] J.L. Chen, X. Yang, Y.D. Li, Fuel 89 (2009) 943–948.
[25] S. Zecevic, E.M. Patton, P. Parhami, Carbon 42 (2004) 1983–1993.
[26] K. Pointon, B. Lakeman, J. Irvine, J. Bradley, S. Jain, J. Power Sources 162 (2006) 750–756.

[27] R.D. Weaver, S.C. Leach, A.E. Bayce, L. Nanis, Direct Electrochemical Generation of Electricity from Coal, SRI, Menlo Park, CA, USA, Report for SAN-0115/105-1, 1979.
[28] G.A. Hackett, J.W. Zondlo, R. Svensson, J. Power Sources 168 (2007) 111–118.
[29] X. Li, Z.H. Zhu, J.L. Chen, R.D. Marco, A. Dicks, J. Bradley, G.Q. Liu, J. Power Sources 186 (2009) 1–9.
[30] L.J. Jia, Y. Tian, Q.H. Liu, C. Xia, J.S. Yu, Z.M. Wang, Y.C. Zhao, Y.D. Li, J. Power Sources doi:10.1016/j.jpowsour.2010.03.016.
[31] D. Cao, Y. Sun, G. Wang, J. Power Sources 167 (2007) 250–257.
[32] N.Z. Muradov, T.N. Veziroğlu, Int. J. Hydrogen Energy 30 (2005) 225–237.
[33] Y.D. Li, R. Zhang, J.L. Chen, X.M. Li, 2nd European Hydrogen Energy Conference, November 2005, Zaragoza, Spain, 2005.
[34] N. Muradov, Int. J. Hydrogen Energy 26 (2001) 1165–1175.
[35] N. Muradov, Catal. Commun. 26 (2001) 89–94.
[36] S. Takenaka, Y. Shigeta, E. Tanabe, K.J. Otsuka, Catalysis 220 (2003) 468–477.
[37] B. Gaudernack, S. Lynum, Proceedings of 11th World Hydrogen Energy Conference, Stuttgart, Germany, 1996.
[38] B.C. Liu, S.H. Tang, L.Z. Gao, Q. Liang, B.L. Zhang, M.Z. Qu, G.Z. Xiong, Z.L. Yu, Chin. J. Catal. 22 (2001) 151–153.
[39] W.Z. Qian, T. Liu, F. Wei, Z.W. Wang, Y.D. Li, Appl. Catal. A 258 (2004) 121–124.
[40] C.H. See, A.T. Harris, Ind. Eng. Chem. Res. 46 (2007) 997–1012.
[41] Q.H. Liu, Y. Tian, C. Xia, L.T. Thompson, B. Liang, Y.D. Li, J. Power Sources 185 (2008) 1022–1029.
[42] J.A. Prins-Jansen, K. Hemmes, J.H.W. De Wit, Electrochim. Acta 42 (1997) 3585–3600.
[43] B. Bosio, P. Costamagna, F. Parodi, Chem. Eng. Sci. 54 (1999) 2907–2916.
[44] L.I. Antroropov, Theoretical Electrochemistry, Mir Publishers, Moscow, 1977.
[45] Q.H. Liu, L.T. Thompson, Y. Tian, C. Xia, L.J. Jia, Y.D. Li, AIChE Annual Meeting, Philadelphia, PA, USA, 2008.
[46] P. Costamagna, K. Honegger, J. Electrochem. Soc. 145 (1998) 3995–4007.
[47] F. Calise, A. Palombo, L. Vanoli, J. Power Sources 158 (2006) 225–244.
[48] G. Hoogers, Fuel Cell Technology Handbook, CRC Press, London, UK, 2002.
[49] S.H. Chan, C.F. Low, O.L. Ding, J. Power Sources 103 (2002) 188–200.
[50] W.H.A. Peelen, M. Olivry, S.F. Au, J.D. Fehribach, K. Hemmes, J. Appl. Electrochem. 30 (2000) 1389–1395.
[51] B.C.H. Steele, Solid State Ionics 134 (2000) 3–20.
[52] J. Palsson, A. Selimovic, L. Sjunnesson, J. Power Sources 86 (2000) 442–448.